DOI: 10.1002/smll.201704526
Article type: Full Paper

Metallic Contact between MoS_2 and Ni via Au Nanoglue

*Xinying Shi, Sergei Posysaev, Marko Huttula, Vladimir Pankratov, Joanna Hoszowska, Jean-Claude Dousse, Faisal Zeeshan, Yuran Niu, Alexei Zakharov, Taohai Li, Olga Miroshnichenko, Meng Zhang, Xiao Wang, Zhongjia Huang, Sami Saukko, Diego López González, Sebastiaan van Dijken, Matti Alatalo, Wei Cao**

X. Shi, S. Posysaev, Prof. M. Huttula, Dr. V. Pankratov, O. Miroshnichenko, Prof. M. Alatalo, Dr. W. Cao
Nano and Molecular Systems Research Unit, University of Oulu, P.O. Box 3000, FI-90014, Finland
E-mail: wei.cao@oulu.fi
Dr. J. Hoszowska, Prof. J.-Cl. Dousse, F. Zeeshan
Department of Physics, University of Fribourg, Ch. du Musée 3, CH-1700 Fribourg, Switzerland
Dr. Y. Niu, Dr. A. Zakharov
MAX IV Laboratory, Lund University, P.O. Box 118, 22100 Lund, Sweden
Prof. T. Li
College of Chemistry, Key Lab of Environment Friendly Chemistry and Application in Ministry of Education, Xiangtan University, Xiangtan 411105, China
Prof. M. Zhang, Prof. X. Wang
Department of Physics, East China University of Science and Technology, Shanghai 200237, China
Prof. Z. Huang
School of Mechanical and Automotive Engineering, Anhui Polytechnic University, Wuhu 241000, China
S. Saukko
Center of Microscopy and Nanotechnology, University of Oulu, P.O. Box 7150, FI-90014, Finland
D. L. González, Prof. S. van Dijken
NanoSpin, Department of Applied Physics, Aalto University School of Science, P.O. Box 15100, FI-00076 Aalto, Finland

Keywords: metallic contact, inorganic layered crystals, synchrotron radiation, first-principles calculations

Abstract:

A critical factor for electronics based on the inorganic layered crystals stems from the electrical contact mode between the semiconducting crystals and the metal counterparts in the electric circuit. Here, a materials tailoring strategy via nanocomposite decoration was carried out to reach metallic contact between MoS_2 matrix and transition metal nanoparticles. Nickel

nanoparticles (NiNPs) were successfully joined to the sides of a layered MoS_2 crystal through gold nano-buffers, forming semiconducting and magnetic NiNPs@MoS_2 complexes. The intrinsic semiconducting property of MoS_2 remain unchanged, and it can be lowered to only few layers. Chemical bonding of the Ni to the MoS_2 host is verified by synchrotron radiation based photoemission electron microscopy, and further proved by first-principles calculations. Following the system's band alignment, new electron migration channels between metal and the semiconducting side contribute to the metallic contact mechanism, while semiconductor-metal heterojunction enhances the photocatalytic ability.

1. Introduction

Since the rediscovery of monolayer graphene,[1,2] exploration and manipulation of layered crystal properties have become a research focus in materials science. Composed of intralayer covalent bonds and interlayer van der Waals interactions, the transition metal dichalcogenides (TMDs) are featured as typical inorganic layered crystals (ILCs). Distinct from the gapless graphene and insulating hexagonal boron nitride (*h*-BN), many TMDs exhibit semiconducting and layer-dependent band structures,[3,4] and thus are considered as promising candidates for future electronics. However, the quality of electrical contact between the ILCs and metals, is of crucial importance to ensure the performance of the entire electronics.[5]

Compared with well-established Group IV semiconductors, effective contacts in ILC-metal systems are rather difficult to achieve, especially in low dimensions.[6] The lack of dangling bonds in pristine ILC surface makes it difficult for bond formation with metals. Thus, contact instability and Schottky barriers with high contact resistance limit the performance of ILC based devices.[7,8] As an intensively studied host matrix, molybdenum disulfide (MoS_2) is a cheap and abundant mineral compared with other TMDs,[9] and is found promising in applications of transistors,[10,11] optoelectronics,[12] catalytic reactions,[13] and even UV-Vis light convertors.[14] It has also been proposed as an alternative to traditional silicon based

semiconductors due to the high mobility and on/off current ratios.[15,16] Furthermore, it has certain photocatalytic abilities in degrading organic pollutants,[17] and the chemical robustness could be enhanced by proper materials engineering.[18] The electronic and catalytic features show great potential for applications in different domains. Despite these achievements, the MoS_2 based electronics or catalysts are barely connected to bulk metal or metal particles in heterojunctional structures.

Indeed, a metal-MoS_2 contact still suffers from high contact resistance induced by Schottky barrier at the interface, limiting the performance of the electronics.[19] To achieve a low resistance contact with MoS_2, the work function (Φ) of selected metals should be smaller than that of MoS_2 (5.2 eV). In this case, an ohmic contact can be formed and electrons can migrate from the metal part and accumulate at MoS_2 conduction band near the contact interface. Among various metals, Ni (Φ = 5.0 eV) and Au (Φ = 5.1 eV) are commonly used as the electrode materials for MoS_2-based electronics.[20,21] Although in practice Fermi level pinning effect hinders the formation of ohmic contacts, these metals are still preferable in MoS_2-based devices.[6] Besides, both Ni and MoS_2 are applicable as 'ink' for conductive lines and patterns in the industry of motherboard printing.[22,23] As a ferromagnetic dopant, nickel also tunes the magnetic property of the Ni-MoS_2 system.[24] Additionally, introducing Ni atoms to MoS_2 matrix enhances structural stability and activates more reaction sites on MoS_2 in practical catalysis.[25] Therefore, incorporating Ni and MoS_2 is promising for wide applications in electronic, magnetic and catalytic aspects.

In this work, we report a materials engineering method via nanocomposite decoration as an efficient and inexpensive way to glue NiNPs to the MoS_2. The key recipe of the synthesis relies on introducing Au nanoglue from chloroauric acid. Through such synthesis, Ni-Au-MoS_2 contact is established with a greatly reduced contact resistance. The synthesized complexes preserve the semiconducting character of the MoS_2 host and the ferromagnetism of Ni. Microscopic and spectroscopic determination from synchrotron based X-ray

photoemission electron microcopy (XPEEM) verified the successful bonding of Ni to the layered MoS_2 at the nanoscale interface regions. The bond formation was supported by charge transfer given in the first-principles calculations. The band alignment was also provided following experimental and computational results. As a result of the semiconductor-metal heterojunction, photocatalytic ability of the MoS_2 is substantially increased. We show that gluing properly selected nanocomposites to the ILCs may provide a general route for transferring the properties of the guest materials to the functionalized host materials, simultaneously reaching metallic contact between the two sites, and improving chemical robustness of the layered hosts.

2. Results

2.1. Morphology

To join NiNPs to the MoS_2 matrix, the preparations were performed through a facile wet chemical synthesis under ultrasonic circumstance. Phonons at ultrasonic frequencies help to evenly mix Ni and MoS_2 powder and provide energy for the synthesis through ultrasonic cavitation.[26] To facilitate the synthesis, chloroauric acid is selected as the oxidative reagent to provide the possible common product of Au in redox reactions. The reduced Au may glue Ni to MoS_2. The step-by-step synthesis protocol is listed in the Experimental Section.

In **Figure 1**a, a nickel particle with a diameter of 200 nm was well joined to the edge of a MoS_2 flake. After 50 times of mechanical exfoliations by Scotch tape, multilayer MoS_2 was thinned down to few layers (Figure 1b), which can be roughly estimated by the contrast between the flakes and the substrates.[27] The NiNP is still well connected to MoS_2 after exfoliation, indicating a strong bonding joining the MoS_2 and Ni. Transmission electron microscope (TEM) was further employed to examine the interface between Ni and MoS_2. Figure 1c shows typical morphology of the synthesized sample that Au nanoparticles are on the edge of multilayer MoS_2 flakes, providing possible sites to hold NiNPs. In this region, the average size of Au nanoparticles is around 50 nm (Figure 1d). It is worth noting that, each Au

particle comprises of several Au crystals. The mean single-crystal size of Au is estimated as 16 nm from X-ray diffraction (XRD) pattern (Figure S1), calculated by the Scherrer equation,[28] consistent with our previous study.[29] Energy dispersive X-ray spectroscopy (EDS) mapping (Figure 1e) and a line-scan (Figure S2) clearly show the distribution of Mo, Au and Ni elements. A high-resolution TEM (HRTEM) image is depicted in Figure 1f. Strong moiré patterns are found here, suggesting the good crystallization and small interlayer lattice offsets of the multilayer MoS_2. The figure also reveals the existence of two types of interfaces. In type-I, the MoS_2 and Ni are connected via Au nanoparticles, as denoted at the lower part of the figure. In contrast, an interface consisting of Mo, Au and Ni is found in the upper side, next to which fringes of Ni (111), Au (111), MoS_2 (100) and (103) are also identified. This type-II interface is further explicated in Figure 1g, with thinner MoS_2 flakes and smaller Au size at another Ni-Au-MoS_2 interface region. The nanocrystallized Au nanoparticles are typically below 5 nm, distributing at both the interface and edges of MoS_2 and Ni. The EDS map (Figure 1h) further proves the overlap of Ni, Mo and Au at the interface. The HRTEM view (Figure 1i) of the same region clearly identifies the existence of the Au (111) nanocrystals between the Ni and MoS_2. The Au crystallized particles correspond to the intensive signals as detected in the EDS. However, no Au fringe is identified in other parts overlapped by Mo, Au and Ni elements, suggesting a possible alloying among the three components.

In the present synthesis route, most Au^{3+} ions are reduced to their neutral state by oxidizing Ni metal, forming the core-shell nanoparticle composites.[30] This can be confirmed through X-ray photoelectron spectroscopy (XPS) in Figure S3. On the MoS_2 site, the chemically active edges promote the reduction of Au^{3+} in solution to neutral Au agglomerations.[29,31] During this process, Mo and S are also partially oxidized. Thus, the Au clusters settle on MoS_2 edges and also attach the introduced NiNPs. On the contrary, NiNPs would not land or attach to the MoS_2 just by mixing. This can be seen in Figure S4, where NiNPs prefer to

aggregate together rather than join MoS_2 flakes. We also explored the versatility of the present synthesis route by changing the MoS_2 flakes to larger MoS_2 and $MoSe_2$ crystals. As shown in Figure S5, NiNPs are successfully decorated on both MoS_2 and $MoSe_2$.

2.2. Electronic properties

It is necessary to check the consistency of semiconducting properties after joining metal nanoparticles. Due to the rather challenging measurement of electric current from nanoscale samples, conductive-AFM (C-AFM) determinations were employed to measure the conductivity.[32] As illustrated in **Figure 2**a, the C-AFM method measures a total electrical resistance of the system, with the contact resistance Ni-Au-MoS_2 included. To focus on the Ni-Au-MoS_2 contact interface, two samples were investigated: Ni joined with MoS_2 via Au nanoglue (Ni-Au-MoS_2 contact) shown in Figure 2b,c, and Ni physically landed on the MoS_2 (Ni-MoS_2 contact) in Figure 2d. Figure 2b shows the SEM image of the Ni-Au-MoS_2 whose chemical composition is further confirmed by EDS (Figure S6). The selected height profile in Figure 2c shows the thickness of MoS_2 flake and the attached Ni particle. With a diameter of ~160 nm, a 300 nm maximum height suggests that the Ni particle does not contact the surface of Au substrate. By probing AFM tip on Ni and applying variable voltages, the current-voltage (*I-V*) curves of these contacts are obtained (Figure 2e). Such *I-V* relations demonstrate that the semiconducting band structure in layered MoS_2 was retained after introducing Au-glued NiNPs.[33]

Using the derivative of the *I-V* curves, the total electrical resistance of sample Ni-Au-MoS_2 (R_{t1}) and Ni-MoS_2 (R_{t2}) can be calculated. The difference between R_{t1} and R_{t2} represents the drop of contact resistance (ΔR_c) between the cases of Ni-Au-MoS_2 and Ni-MoS_2, as shown in Figure 2f. Barrier heights of the metal-semiconductor contact decrease with the voltage,[20,34] resulting in a significant fall of R_c. In the case of Ni-Au-MoS_2 contact, R_c is reduced by 91.9±2.5% at 5 V. The contact resistivity is also estimated (see Figure S7). At the voltage of 5 V, the electrical resistivity of direct Ni-MoS_2 contact is 46.3 Ω·mm, in good agreement with a

previously reported value of 38 Ω·mm between the Ni electrode and MoS_2.[20] Different from the case of Ni-MoS_2, the contact after introducing Au nanoglue reduces the resistivity down to 3.7 Ω·mm.

2.3. Magnetic properties

The magnetic property from the guest metal is preserved in the newly formed heterojunctions. After successful decoration of NiNPs on MoS_2, potential applications of such complexes may depend on the magnitude of the magnetic moments brought in by the NiNPs. To characterize the magnetic properties, the complexes were dried from suspension and measured by vibrating sample magnetometry (VSM) at room temperature. Unlike diamagnetic MoS_2 (**Figure 3**a), a nearly closed magnetic hysteresis curve is measured on Ni-decorated MoS_2 (Figure 3b). As a reference, we also measured pure NiNPs (Figure 3c). The saturation magnetization of the NiNPs amounts 51.4 emu/g, which corresponds closely to the Ni bulk value of 57.8 emu/g. Considering the weight percentage of Ni, the measured saturation magnetization of 4.6 emu/g suggests that the Ni nanoparticles retain their magnetic properties upon gluing to MoS_2. The small remanent magnetic moments of both the NiNPs and NiNPs@MoS_2 indicate that the particles exhibit a multidomain state, which is typical for NiNPs with diameters exceeding 80 nm.[35]

2.4. Bonding determination from synchrotron radiation based XPEEM

The extremely small interfacial contact between NiNPs and MoS_2 demands simultaneous microscopic and spectroscopic determinations to verify the bond mechanism at the interface. For this reason, we employed synchrotron radiation based XPEEM, and measured the X-ray absorption spectroscopy (XAS) spectra from different sites of the heterojunctions. Due to the relatively low magnification of the XPEEM, the region of interest (ROI) for the XPEEM was preselected by using SEM with higher spatial resolution. The SEM image is shown in **Figure 4**a. Similar to those shown before, the NiNPs@ILC is composed of Ni particles decorated on

layered MoS_2 flakes. The EDS result in Figure 4b further proved the coexistence of Ni, MoS_2 and Au nanoglue.

The ROI was identified and investigated through XPEEM. Shown in the center of the PEEM image in Figure 4c and zoomed-in in Figure 4d, the complex at the ROI kept the shape and location as these in SEM (See the full view of original and rotated PEEM images in Figure S8). By tuning the synchrotron beam energy from 845 eV to 875 eV, the XAS covered the main features of Ni 2*p* $L_{2,3}$ edges. A general XAS survey of the whole region given covered by the zoom is depicted at the bottom of Figure 4e. Apparently, the XAS resembles the one of nickel metal, denoting the stability of the NiNPs during the chemical synthesis.[36] By picking the XAS signal at specific locations, regional chemical environment of the nickel can be identified. At the edge of the heterojunction where a NiNP locates (cycled in cyan at Figure 4a), the XAS denotes the particle is a neutral NiNP, as shown in Figure 4d (blue spectrum). However, for the XAS spectra collected from regions of the joint between Ni and MoS_2, a small peak turns out at the photon energy of 861 eV. The unexpected peak is attributed to signals from Ni atoms bonded with S but subjected to confined spaces,[37] and also observed in the XAS from nickel chalcogenide nano films.[38] Furthermore, this peak is more pronounced once collected from Region 1 where a larger nodule locates between the semiconductor and metal sites. Compared with Region 2 where the connection is rather flat, the nodule may refer to a larger quantity of bonded Ni subjected to ultrasonic reaction after breaking of original bonds in the ILC with the existence of Au glue. Remarkably, the sample is stable subjected to radiations from synchrotron and electron beam (see details in Figure S9).

3. Discussion

Density functional theory (DFT) calculations were employed to explicate the complex growth mechanism, and the origins of the materials properties. Based on morphological determinations in Figure 1, two models were constructed. Each one contains a 3×1×4 unit cell of the MoS_2 host. To reach a reasonable computational time for model-I (type-I contact), the

nanocrystallized Au nanoglue was simplified to 4 layers of Au atoms between the Ni and MoS_2 sides. Two contact layers are relaxed for structural optimizations at each side, and another two fixed as Au (111). The second model (type-II) employs the interfacial characters where the Au and Ni atoms are randomly placed to reach possible alloying. The Ni (111) is connected to the interface, opposite to the MoS_2.

The full model of model-I has a supercell of $Mo_{24}S_{48}Au_{46}Ni_{92}$ (Figure S10), where the thickness of each slab of Ni (111), Au (111) and MoS_2 is around 1 nm. For clarification of the metal-semiconductor contact region and comparison with another model, we present the contact region consisting of MoS_2 and two layers of gold in **Figure 5**a. The partial density of states (PDOS) of Mo and S atoms subjected to the Au adsorption is shown in Figure 5b. After adsorbing gold atoms, structural relaxation is small at the host side. The guest gold buffer tends to be adsorbed by the ideal MoS_2 edge, forming a contact with the host. The charge density difference clarifies the charge transfer between the gold layer and the MoS_2 side, as shown in Figure S11. The non-zero PDOS (grey line in Figure 5b) of the host disperses crossing the Fermi level, denoting a total metallization via side contact after introduction of the gold slab. This is different from the bare MoS_2 side whose PDOS (red line in Figure 5b) suffers from discontinuity around the Fermi-level, as pointed out by the green regions in the figure.

The optimized structure of the model-II is depicted in Figure 5c, with a supercell of $Mo_{24}S_{48}Au_6Ni_{72}$. The edge of Ni (111) is finished with randomly distributed nickel atoms, following the HRTEM observation in Figure 1i. After structural optimization, the Au atoms diffuse between the metal and MoS_2 sides, and attract electron charge from both sides as shown by the charge differences in Figure S11. The Ni atoms are also dragged to the MoS_2 side and charge transfer happens between the Ni and S atoms as shown in the figure. As a consequence, this may contribute to the bonding between the Ni and S atoms at the squeezed space as indicated by the additional peak in the PEEM observations. Similar to model-I,

model-II also leads to metallization of the MoS_2 after metal adsorptions. The PDOS in Figure 5d is fully filled with states near Fermi level due to existence of Ni and Au atoms. In brief, introducing the Au buffer or Au-Ni alloy at the edges enables the metallization of the MoS_2 side, in line with the previous theoretical prediction of side contact to monolayer MoS_2.[39]

Separate spin-polarized calculations were also carried out for bulk Ni, MoS_2-Ni and Au-Ni interfaces, with various percentage of Ni substitutions (0, 8, 16%). The calculated magnetic moment of bulk nickel is 0.67 μ_B, in good agreement with VSM results. Reduction of magnetic moment of nickel was observed on atoms in contact with Au (111) down to 0.44 μ_B and with MoS_2 (100) surface down to 0.2 μ_B. Small magnetic moments were found on Mo, S and Au atoms as well.

Introducing the Au-Ni alloy onto the MoS_2 side will offer new electron migration channels between the metal and the semiconductor side, leading to a metallic contact mechanism. This has been shown in the PDOS of two models where the MoS_2 side owns electronic structures similar to metals. Different from the structure of its semiconductive bulk counterpart in previous studies,[14] the side surface of the MoS_2 has rich but not overlapped bands. Contact between the Ni metal and MoS_2 is metallic since significant electron state overlap was found, smearing the gap between conduction and valence bands and avoiding tunnel barriers. This leads to a different *I-V* feature from the physically adsorbed Ni-MoS_2 counterpart as shown in Figure 2.

A band alignment scheme is illustrated in Figure 5e following the above experimental and theoretical results. When NiNPs and MoS_2 are joined by Au buffers, free electrons will transfer from Ni to MoS_2 via Au due to the work function difference, leading to the accumulation of electrons in the valence band of MoS_2 adjacent to the interface region. The Fermi levels of the Ni, MoS_2 and the interface region will be aligned after thermodynamic equilibrium,[40] resulting in the band bending of MoS_2. Electrons are shared between the NiNPs and Ni-Au-MoS_2 interfaces, and smoothly barred by MoS_2 bulk. On the other hand,

electrons can migrate reversely thanks to the metallic contact, from the semiconductor valence band (VB) to the metal part. This was verified by the photocatalytic degradation of methylene blue (MB). The synthesized MoS_2-Au-Ni ternary complex as well as Au-decorated MoS_2 and commercial MoS_2 are used to degrade MB under UV light irradiation (Figure S12). During photolysis process (without catalyst, see the blank curve), the concentration of MB is kept nearly unchanged, suggesting that the self-degradation is slow even when exposed under UV light. Commercial MoS_2 and Au-decorated MoS_2 show weak photocatalytic ability. In the case of NiNPs@MoS_2, the concentration of MB reduces drastically during the first 30 min, and is almost eliminated after 90 min. During the photocatalytic process, the photogenerated electrons from VBs of MoS_2 reach its conduction bands (CB), then move through the interface to NiNPs at a lower energy. The holes (h^+) in the VBs can hardly pop up to the metal part through an energetically lower basin. The h^+ oxidizes water to form H^+ and hydroxyl radicals OH· which can oxidize the organic dye directly. The photoexcited electrons can move easily from the VB of MoS_2 to the metal side, and reduce the H^+ to H·. Thus, electron-hole recombination in the semiconductive catalyst is inhibited.[41]

4. Conclusion

In conclusion, with the proposed synthesis method, an effective metallic contact is established between MoS_2 and NiNPs, introducing ferromagnetic and enhanced photocatalytic properties. Samples both in suspension and in dry powder form are feasible to prepare, thus suitable for industrial production. Endowed with magnetic attribute, such TMDs provide high potential for innovation in semiconductor industry, and provide a series of candidates for chemical catalysts. The synthesis route was also proven efficient in joining different TMDs to NPs. The growth mechanism was explicated in first-principles calculations. Through the present experimental evidence and theoretical clarifications, the side contact model was realized. Further investigations may also pay attention to targeted doping to particular

positions of semiconductor layers, and extend the present method to synthesize ILC-based materials for specific needs.

5. Experimental Section

Synthesis and sample preparation: MoS_2 flake powders (>99.5%) were purchased from Nanjing Emperor Nano Material Co. Ltd. and guaranteed reagent $HAuCl_4 \cdot 4H_2O$ (Au content >47.8%) from Yurui Chemistry Co. Ltd. Nickel powder of an average diameter of 200 nm was produced by reduction sintering from nickel oxalate. The synthesis of Ni-Au-MoS_2 complexes was carried out with the following protocols. Step 1: Mix MoS_2 powder (43.4 mg) and Ni powder (4 mg) in a Duran Erlenmeyer flask (capacity: 100 mL). Step 2: Add ultrapure water (Millipore, 18.2 MΩ·cm @ 25 ºC) to the flask. Seal with a stopper and then shake the flask vigorously to get evenly dispersed suspension. Step 3: Remove the stopper and blow Ar gas to the suspension for 5 minutes to remove the oxygen dissolved in the suspension and in the air. Step 4: Add $HAuCl_4$ aqueous solution (1.3 mL, 0.01 $mol \cdot L^{-1}$) to the flask and immediately seal it. Step 5: Put the flask in an ultrasonic cleaner (35kHz, 50 °C) for 30 minutes. Step 6: After synthesis, turn off the ultrasonic cleaner. Keep the flask in the cleaner and let it cool down to room temperature. Samples with nominal weight percentages of $(MoS_2)_{86.7}Ni_8Au_{5.3}$ was then synthesized. Step 7: Keep the flask still for one day, then remove the remaining water in the upper part. Wash the synthesized complexes by ultrapure water. Samples of $(MoS_2)_{92.9}Ni_{4.2}Au_{2.9}$, $(MoS_2)_{94.2}Ni_{4.3}Au_{1.5}$, and $(MoS_2)_{89.1}Ni_{8.2}Au_{2.7}$ were synthesized in the same way. A control group of samples were synthesized with HCl instead of $HAuCl_4$. The amount of MoS_2, Ni and Cl^- were kept the same in each group.

The synthesized product was then dispersed in ethanol (Sigma-Aldrich, 95.0%). Use a pipette to take several drops of the suspension and then drip onto various substrates for different characterizations. The remaining ethanol after deposition was removed by evaporation. For normal SEM and XPS measurements, the suspension was deposited on pure silicon substrate. To obtain thin layer flakes under SEM, Scotch tape exfoliation of 30 ~ 50

times was carried out before SEM tests. For C-AFM tests, a gold film (30 nm thick) was coated on silicon substrates for better electrical conductivity. The Au film is also excellent for thermal conduction, beneficial to ease the thermal effect on the resistivity. The substrate was put on a thin steel sheet with Au side upwards. The Au film and steel sheet were connected by conductive glue. The suspension was then deposited on the Au film. In order to compare with Ni-Au-MoS_2 contact, a Ni-MoS_2 contact was fabricated by firstly coating a layer of pure MoS_2 on Au film and then depositing Ni nanoparticles on top of MoS_2 layer. For TEM tests, suspension was deposited on a lacey carbon film (Agar Scientific Ltd.). For XRD measurements, the suspension was deposited onto a misoriented silicon wafer. For XPEEM experiments, the suspension was deposited on germanium substrates for better electrical conductivity.

SEM, TEM, XRD and XPS characterizations: Microscopy characterizations were studied with a ZEISS Sigma FESEM and a JEOL JEM-2200FS EFTEM/STEM. In XRD measurements, a monochromatized Cu K_α X-ray tube was used as the incident source. A rough scan was firstly performed from 10° to 60°, and a long time scan followed in the range of 35° ~ 53°. XPS measurements were performed with a Thermo Fisher Scientific ESCALAB 250Xi XPS system with Al K_α X-ray source.

I-V measurements: Current-voltage measurements were performed under Veeco Dimension 3100 atomic force microscope. For each sample, morphologies were always firstly obtained under tapping mode with a NSC18 tip (MIKROMASCH). *I-V* measurements were then carried out under Force mode, and the tip was changed to a Veeco MESP one with conductive Co/Cr coating. The C-AFM technique measures a total electrical resistance including contact resistance of tip-Ni, Ni-Au-MoS_2, MoS_2-Au substrate and intrinsic resistance of Ni, MoS_2 and the AFM machine. Thus the individual contact of Ni-Au-MoS_2 can be evaluated by comparing with a direct Ni-MoS_2 sample. The difference between total resistances of the two cases (R_{t1}, R_{t2}) represents the decrease of contact resistance (ΔR_c). Since contact area of

MoS_2-Au film is much larger than the Ni-MoS_2 interface, its resistance is negligible compared to R_{t2}. Therefore, the R_c drop can be estimated by $\Delta R_c/R_{t2}$. The reliability of the *I-V* measurements was checked in Figure S13. The contact force keeps stable (~30 nN) when the setpoint voltage varies from 0.1 V to 3.0 V. It ensures that the tip-Ni resistance is constant during the measurements. A short circuit test was also performed (Figure S14), demonstrating a good electrical connection between the substrate and AFM sample holder.

Magnetic measurements: The magnetic properties of $(MoS_2)_{92.9}Ni_{4.2}Au_{2.9}$ and commercial MoS_2 were measured using a physical properties measurement system (PPMS) from Quantum Design (Dynacool 9 T) with a VSM option. Dry powder for magnetic characterization was obtained by evaporating the suspension at 130 ºC in a vacuum oven dryer.

XPEEM: XAS measurements were investigated at PEEM endstation of Beamline I311 at Max IV laboratory (Lund, Sweden). Samples were degassed and discharged in an ultrahigh vacuum chamber before exposed to synchrotron photons. The energy resolution was estimated to > 2000 and flux ~ 10^{12} ph./s by utilizing a modified SX-700 monochromator with a Si 1200 line/mm grating for the Ni 2*p* $L_{2,3}$ edge. Mechanic backslashes were negligible thanks to the reliability of the beamline optics. The Ni 2*p* XAS spectra were recorded from 845 ~ 875 eV, with a 0.2 eV step. Each step took 16 frames of images (exposed 4 seconds per frame). The selected regions were zoomed to 25 μm in stack and consisted of 1200×1200 pixels. The secondary electron signals through a multi-channel plate (MCP) were recorded for the total electron yields (TEY). More details of the measurements can be found in previous experiments.[42]

Photocatalytic measurements: Degradation measurements were performed under UV light (UV lamp, 500W) irradiation. During each measurement, $(MoS_2)_{92.9}Ni_{4.2}Au_{2.9}$ sample (50 mg) and MB (50 mL, 10 mg·L^{-1}) were mixed and then the suspensions were magnetically stirred in the dark for 30 min to eliminate the equilibrium effects before the irradiation. 5mL suspension was taken out in every 30 min, and centrifuged for 5 min. The supernatants were

collected then. The residual concentration of MB was measured through a Lambda 25 UV-vis spectrophotometer (Perkin-Elmer, USA). The same tests were also done with MoS_2-Au and commercial MoS_2.

Computational details: First-principles calculations were performed with DFT, using the projector augmented wave method as implemented in Vienna Ab initio Simulation Package (VASP).[43,44] The plane wave cut-off energy was set to 400 eV. The Perdew-Burke-Ernzerhof functional was used to treat the electron exchange and correlations, together with van der Waals (DFT-D3) correction.[45,46] The convergence criterion was chosen so that the maximum force on one atom is smaller than 0.02 eV/Å. The calculations were performed with periodic boundary conditions. The vacuum region in the z-direction was set to 15 Å to avoid mirror interactions between nearby images. During relaxation all atoms were allowed to relax except for: in model-I, two middle layers of gold, which represent the bulk of gold; and in model-II, two bottom layers of MoS_2, which represent the bulk of MoS_2.

The Brillouin zone was sampled using a Monkhorst-Pack k-point set containing 4×1×2 k-points during the structural optimization and PDOS calculation.[47] For band structure calculation, 30 k-points were used along a special k-point path in the Brillouin zone. Spin-polarized calculations were also carried out to obtain magnetic properties. The plotting of 3D isosurfaces for the $\Delta\rho$ function was performed using the VESTA3 code,[48] and the VMD code was used for the schematic diagram of the *I-V* measurement.[49] The calculations are consistent with those using other software packages,[50,51] as well as results crosschecked with experimental determinations.[14]

Supporting Information

Supporting Information is available from the Wiley Online Library or from the author.

Acknowledgements

We acknowledge financial support from Strategic Grant of University of Oulu, National Natural Science Foundation of China (Grant No. 11204079), and the Natural Science

Foundation of Shanghai (Grant No. 12ZR1407000). W.C. and M.H. acknowledge the European Regional Development Funding and the Oulu Council. X.S. acknowledges the scholarship sponsored by China Scholarship Council. J.H., J.-Cl.D. and F.Z. acknowledge the financial support of the Swiss National Science Foundation (Grant No. 200020_146739). The authors thank the Center of Microscopy and Nanotechnology of University of Oulu. Computing resources were provided by CSC - IT Centre for Science Ltd. The research leading to these results has received funding from the European Commission's Seventh Framework Programme (FP7/2007–2013) CALIPSO under Grant Agreement No. 312284. The authors thank also the crew of the MAX IV laboratory for their support during the beamtime operation.

Received: ((will be filled in by the editorial staff))

Revised: ((will be filled in by the editorial staff))

Published online: ((will be filled in by the editorial staff))

References

[1] K. S. Novoselov, A. K. Geim, S. V. Morozov, D. Jiang, Y. Zhang, S. V. Dubonos, I. V. Grigorieva, A. A Firsov, *Science* **2004**, *306*, 666.

[2] K. S. Novoselov, A. K. Geim, S. V. Morozov, D. Jiang, M. I. Katsnelson, I. V. Grigorieva, S. V. Dubonos, A. A. Firsov, *Nature* **2005**, *438*, 197.

[3] M. Chhowalla, H. S. Shin, G. Eda, L.-J. Li, K. P. Loh, H. Zhang, *Nat. Chem*. **2013**, *5*, 263.

[4] C. Tan, X. Cao, X.-J. Wu, Q. He, J. Yang, X. Zhang, J. Chen, W. Zhao, S. Han, G.-H. Nam, M. Sindoro, H. Zhang, *Chem. Rev*. **2017**, *117*, 6225.

[5] S. Manzeli, D. Ovchinnikov, D. Pasquier, W. V. Yazyev, A. Kis, *Nat. Rev. Mater*. **2017**, *2*, 17033.

[6] A. Allain, J. Kang, K. Banerjee, A. Kis, *Nat. Mater*. **2015**, *14*, 1195.

[7] W. Wu, L. Wang, Y. Li, F. Zhang, L. Lin, S. Niu, D. Chenet, X. Zhang, Y. Hao, T. F. Heinz, J. Hone, Z. L. Wang, *Nature* **2014**, *514*, 470.

[8] I. Popov, G. Seifert, D. Tomanek, *Phys. Rev. Lett.* **2012**, *108*, 156802.

[9] J. Y. Park, H.-E. Joe, H. S. Yoon, S. Yoo, T. Kim, K. Kang, B.-K. Min, S. C. Jun, *ACS Appl. Mater. Interfaces* **2017**, *9*, 26325.

[10] H. Li, Z. Yin, Q. He, H. Li, X. Huang, G. Lu, D. W. H. Fam, A. I. Y. Tok, Q. Zhang, H. Zhang, *Small* **2012**, *8*, 63.

[11] B. Radisavljevic, A. Radenovic, J. Brivio, V. Giacometti, A. Kis, *Nat. Nanotech*. **2011**, *6*, 147.

[12] O. Lopez-Sanchez, D. Lembke, M. Kayci, A. Radenovic. A. Kis, *Nat. Nanotech*. **2013**, *8*, 497.

[13] J. Kibsgaard, Z. Chen, B. N. Reinecke, T. F. Jaramillo, *Nat. Mater*. **2012**, *11*, 963.

[14] V. Pankratov, J. Hoszowska, J.-Cl. Dousse, M. Huttula, A. Kis, D. Krasnozhon, M. Zhang, W. Cao, *J. Phys.: Condens. Matter* **2016**, *28*, 015301.

[15] K. F. Mak, C. Lee, J. Hone, J. Shan, T. F. Heinz, *Phys. Rev. Lett*. **2010**, *105*, 136805.

[16] R. Ganatra, Q. Zhang, *ACS Nano* **2014**, *8*, 4074.

[17] T. R. Thurston, J. P. Wilcoxon, *J. Phys. Chem. B* **1999**, *103*, 11.

[18] H. Li, C. Tsai, A. L. Koh, L. Cai, A. W. Contryman, A. H. Fragapane, J. Zhao, H. S. Han, H. C. Manoharan, F. Abild-Pedersen, J. K. Nørskov, X. Zheng, *Nat. Mater.* **2016**, *15*, 48.

[19] S. Das, H.-Y. Chen, A. V. Penumatcha, J. Appenzeller, *Nano Lett*. **2013**, *13*, 100.

[20] W. S. Leong, X. Luo, Y. Li, K. H. Khoo, S. Y. Quek, J. T. L. Thong, *ACS Nano* **2015**, *9*, 869.

[21] L. Yang, K. Majumdar, H. Liu, Y. Du, H. Wu, M. Hatzistergos, P. Y. Hung, R. Tieckelmann, W. Tsai, C. Hobbs, P. D. Ye, *Nano Lett*. **2014**, *14*, 6275.

[22] J. Perelaer, P. J. Smith, D. Mager, D. Soltman, S. K. Volkman, V. Subramanian, J. G. Korvink, U. S. Schubert, *J. Mater. Chem*. **2010**, *20*, 8446.

[23] J. Li, M. M. Naiini, S. Vaziri, M. C. Lemme, M. Östling, *Adv. Funct. Mater.* **2014**, *24*, 6524.

[24] A. N. Andriotis, M. Menon, *Phys. Rev. B* **2014**, *90*, 125304.

[25] J. Miao, F.-X. Xiao, H. B. Yang, S. Y. Khoo, J. Chen, Z. Fan, Y.-Y. Hsu, H. M. Chen, H. Zhang, B. Liu, *Sci. Adv*. **2015**, *1*, e1500259.

[26] Z. He, W. Que, *Appl. Mater. Today* **2016**, *3*, 23.

[27] M. M. Benameur, B. Radisavljevic, J. S. Héron, S. Sahoo, H. Berger, A. Kis, *Nanotechnology* **2011**, *22*, 125706.

[28] U. Holzwarth, N. Gibson, *Nat. Nanotech*. **2011**, *6*, 534.

[29] W. Cao, V. Pankratov, M. Huttula, X. Shi, S. Saukko, Z. Huang, M. Zhang, *Mater. Chem. Phys*. **2015**, *158*, 89.

[30] R. G. Chaudhuri, S. Paria, *Chem. Rev*. **2012**, *112*, 2373.

[31] S. M. Tan, A. Ambrosi, Z. Sofer, Š. Huber, D. Sedmidubský, M. Pumera, *Chem. Eur. J.* **2015**, *21*, 7170.

[32] J. Liu, A. Goswami, K. Jiang, F. Khan, S. Kim, R. McGee, Z. Li, Z. Hu, J. Lee, T. Thundat, *Nat. Nanotech*. **2018**, *13*, 112.

[33] S. Zorba, Q. T. Le, N. J. Watkins, L. Yan, Y. Gao, *J. Nanosci. Nanotech*. **2001**, *1*, 317.

[34] N. Kaushik, A. Nipane, F. Basheer, S. Dubey, S. Grover, M. M. Deshmukh, S. Lodha, *Appl. Phys. Lett*. **2014**, *105*, 113505.

[35] A. G. Kolhatkar, A. C. Jamison, D. Litvinov, R. C. Willson, T. R. Lee, *Int. J. Mol. Sci.* **2013**, *14*, 15977.

[36] F. Lin, D. Nordlund, T. Pan, I. M. Markus, T.-C. Weng, H. L. Xin, M. M. Doeff, *J. Mater. Chem. A* **2014**, *2*, 19833.

[37] T. Kroll, R. Kraus, R. Schönfelder, V. Y. Aristov, O. V. Molodtsova, P. Hoffmann, M. Knupfer, *J. Chem. Phys*. **2012**, *137*, 054306.

[38] J. D. Aldous, C. W. Burrows, I. Maskery, M. Brewer, D. Pickup, M. Walker, J. Mudd, T. P. A. Hase, J. A. Duffy, S. Wilkins, C. Sánchez-Hanke, G. R. Bell, *J. Cryst. Growth* **2012**, *357*, 1.

[39] J. Kang, W. Liu, D. Sarkar, D. Jena, K. Banerjee, *Phys. Rev. X* **2014**, *4*, 031005.

[40] Z. Zhang, J. T. Yates Jr., *Chem. Rev*. **2012**, *112*, 5520.

[41] S. Zhu, Q. Li, F. Li, W. Cao, T. Li, *J. Phys. Chem. Solids* **2016**, 92, 11.

[42] W. Cao, V. Pankratov, M. Huttula, L. Shirmane, Y. R. Niu, F. Wang, *Surf. Rev. Lett*. **2014**, *21*, 1450058.

[43] G. Kresse, D. Joubert, *Phys. Rev. B* **1999**, *59*, 1758.

[44] G. Kresse, J. Furthmüller, *Phys. Rev. B* **1996**, *54*, 11169.

[45] J. P. Perdew, K. Burke, M. Ernzerhof, *Phys. Rev. Lett.* **1996**, *77*, 3865.

[46] S. Grimme, J. Antony, S. Ehrlich, H. Krieg, *J. Chem. Phys*. **2010**, *132*, 154104.

[47] H. J. Monkhorst, J. D. Pack, *Phys. Rev. B* **1976**, *13*, 5188.

[48] K. Momma, F. Izumi, *J. Appl. Crystallogr*. **2011**, *44*, 1272.

[49] W. Humphrey, A. Dalke, K. Schulten, *J. Mol. Graphics* **1996**, *14*, 33.

[50] J. Vähäkangas, P. Lantto, J. Vaara, M. Huttula, W. Cao, *Chem. Commun*. **2017**, *53*, 5428.

[51] M. Zhang, Z. Huang, X. Wang, H. Zhang, T. Li, Z. Wu, Y. Luo, W. Cao, *Sci. Rep*. **2016**, *6*, 19504.

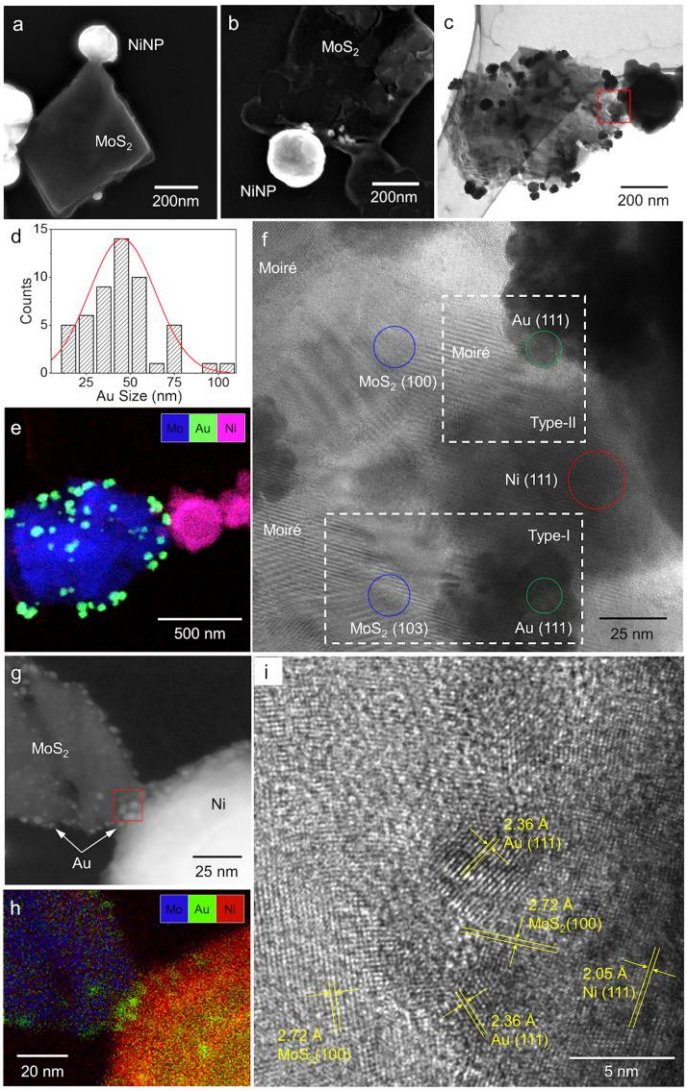

Figure 1. Morphologies of MoS_2-Ni complexes glued by Au nanoparticles. a) Scanning electron microscope (SEM) image shows a well-shaped MoS_2 flake with a Ni nanoparticle on the edge. b) SEM image taken after 50 times of mechanical exfoliation. c) TEM image. d) Histogram of Au nanoparticle size distribution in (c). e) TEM-EDS mapping. f) HRTEM of the square region shown in (c). The lower and upper rectangles in dash line denote the type-I and type-II interfaces, respectively. g) Dark field TEM image showing Au nanoparticles in a smaller size. h) TEM-EDS mapping. i) HRTEM of the square region shown in (g).

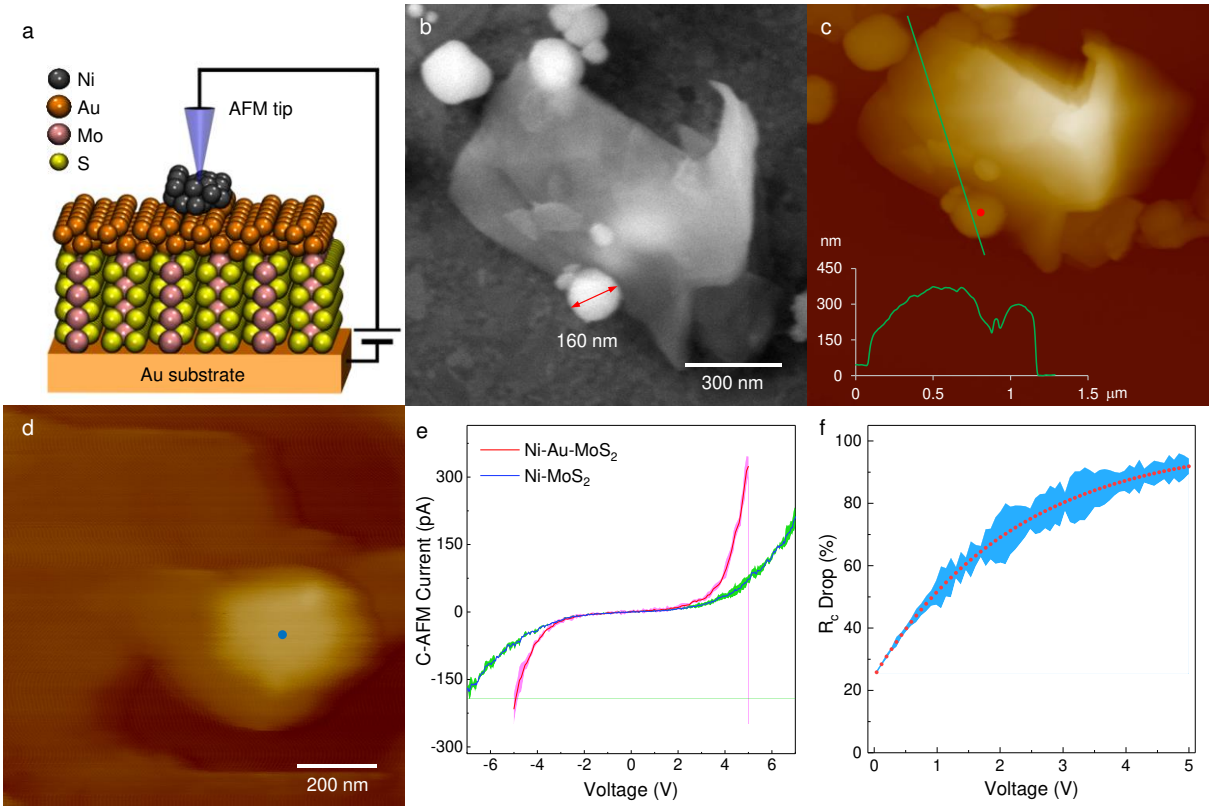

Figure 2. Electrical characterization by C-AFM. a) Schematic diagram of the *I-V* measurement. b) SEM image of an isolated sample. c) AFM image of the sample shown in (b). A Ni nanoparticle positions at the edge of MoS_2 with Au in between. The inset shows a height profile of the sample. d) Ni deposited directly on MoS_2. e) *I-V* curves. The red and blue curves were measured at the red point in (c) and blue point in (d), respectively. (f) R_c drop compared between the cases of Ni-Au-MoS_2 contact and Ni-MoS_2 contact. The shadings represent standard deviations in (e) or measurement uncertainty in (f).

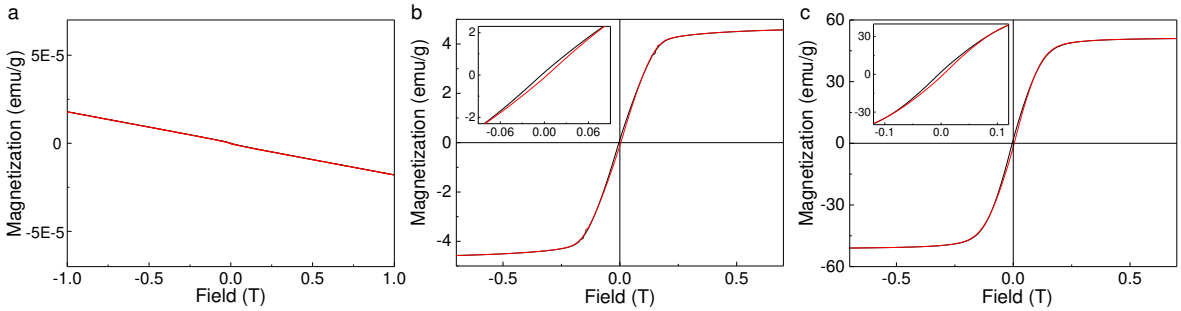

Figure 3. Room temperature magnetic hysteresis loops. a) MoS_2, b) NiNPs@MoS_2, c) Pure NiNPs. Insets in (b) and (c) are zoomed-in parts of the loops.

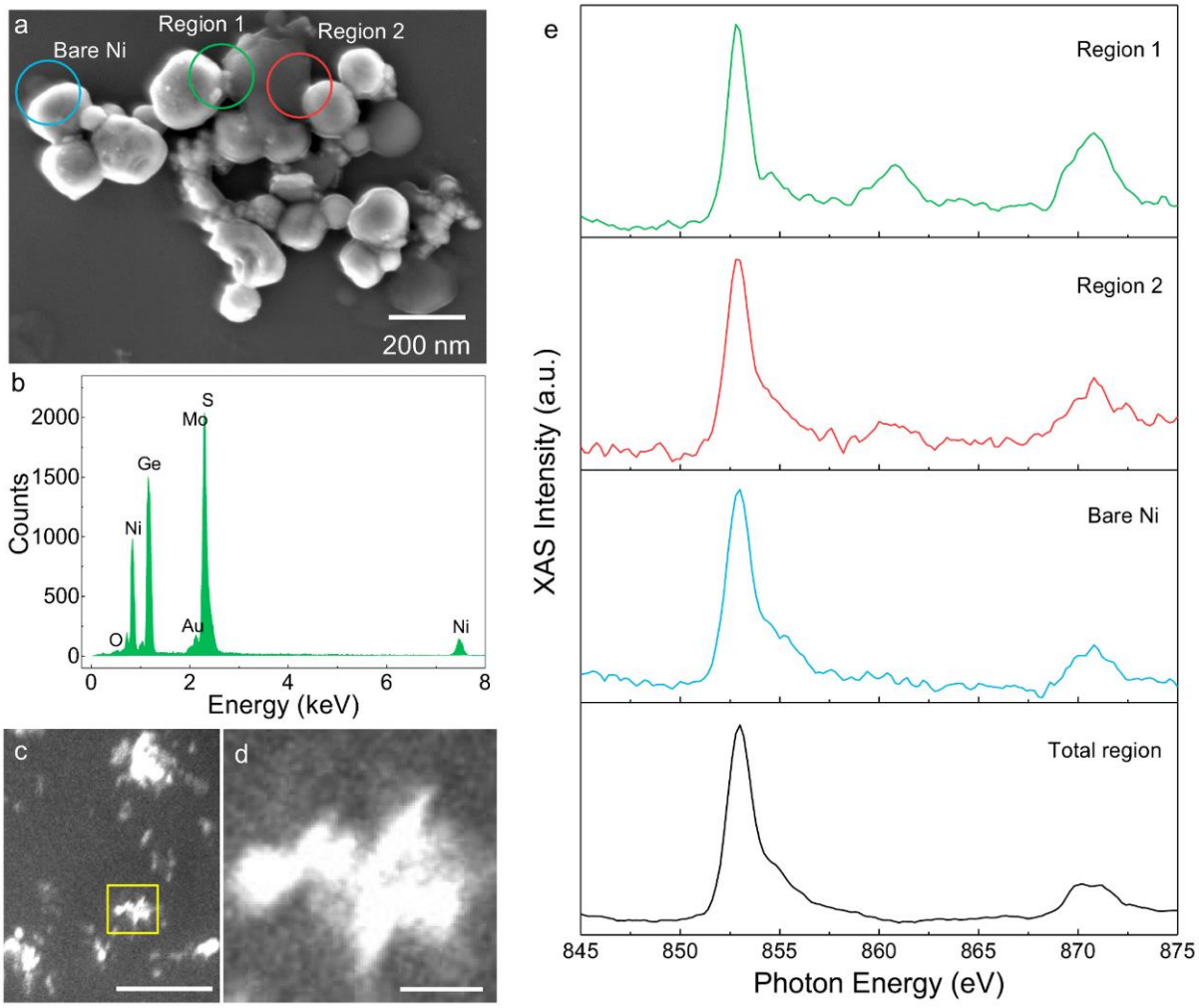

Figure 4. XAS investigations of the synthesized complexes. a) SEM image shows zoomed-in details of the selected region. Three nano regions are marked with circles (diameter: 175 nm) of different colors: cyan (bare Ni), green (interfacial region 1), red (interfacial region 2). b) EDS spectrum of region 1. The Ge peak comes from germanium substrate, which is specifically used for better electrical conductivity. c) XPEEM image. d) Zoomed-in view of the square region marked in (c). Both panel (c) and (d) were rotated 125° anticlockwise from the original PEEM view. Scale bars in (c) and (d) are 3 μm and 500 nm, respectively. e) XAS spectra of region 1, region 2, bare Ni, and the marked region in (c), respectively.

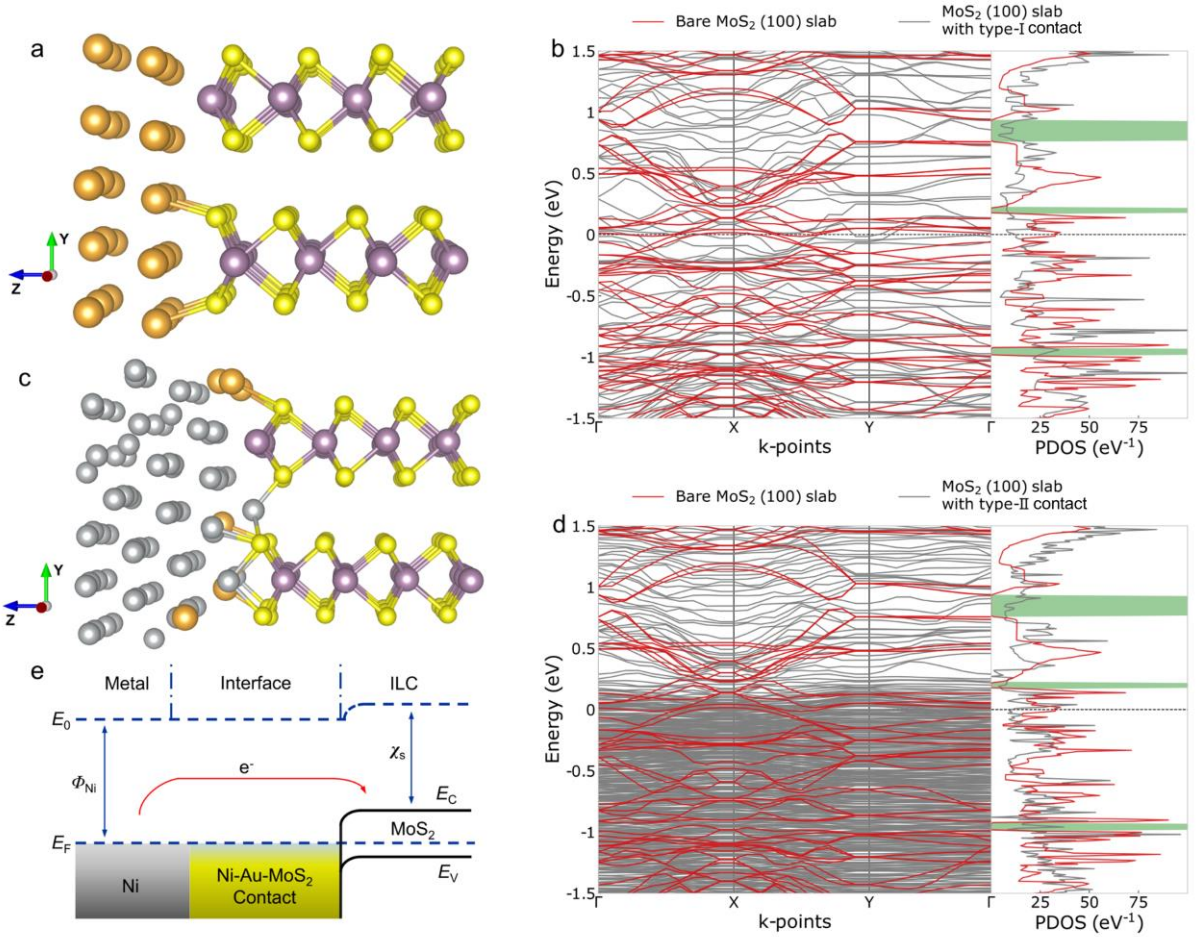

Figure 5. Geometric and electronic structures. a) Optimized geometry of the $Mo_{24}S_{48}Au_{30}$ supercell. b) Band structure of the MoS_2 (100) surface without contact is plotted with red curves, while gray curves represent band structure of Au-MoS_2 interface in model-I. c) Optimized geometry of the $Mo_{24}S_{48}Au_6Ni_{72}$ supercell. d) Band structure of the edge surface of MoS_2 without contact is plotted with red curves, while gray curves represent band structure for type-II contact. In panel (a) and (c), the silver, orange, purple and yellow spheres represent the Ni, Au, Mo and S atoms, respectively. PDOS represent the sum over all Mo and S atoms, and green regions show empty states for MoS_2 (100) surface. e) Band alignment at metal-semiconductor interface. E_0, E_F, E_C, E_V, Φ_{Ni}, and χ_s represent the vacuum level, Fermi level of metal, the conduction and valence band of MoS_2, the work function of Ni, and the electron affinity of MoS_2, respectively.